Multiscale local Map Drift driven Multilateration SAR Autofocus using fast Polar Format Image Synthesis.

Hubert M.J. Cantalloube

Office National d'Études et Recherches Aérospatiales, Chemin de la Hunière 91120 Palaiseau, France
tél +33 1 69 93 62 12, fax +33 1 69 93 62 69, http://phare.normalesup.org/~cantallo/index.html,
cantallo@onera.fr

Carole E. Nahum

Direction Générale de l'Armement, 5 rue des Mathurins 92221 Bagneux, France

Abstract

This new autofocus is based on multilateration by ranging to small target areas at independent directions on the ground. Range-clipped Doppler low-filtered profiles around target points are used to compute local images using frequency domain polar format algorithm. Images obtained from adjacent subapertures are registered and the displacements yields elevation, trajectory or clock drifts (bistatic case) errors. To alleviate the insensitivity of map-drift to error fluctuation faster than sub-aperture duration, algorithm is reiterated with coarse-to-fine resolution yielding high to low frequency errors. This allowed true bistatic SAR autofocus (without monostatic image) and our first successful air-to-air ISAR high resolution imaging.

1 Context

Low to medium (1 m to 30 cm) resolution SAR imaging at ONERA in the 80's and 90's (before high accuracy GPS-hybridized IMU allowed direct SAR synthesis from measured trajectory) used local map-drift autofocus. This technique, measuring distorsion field between two (or more) independent looks (stripmap images) produced estimates in low frequency trajectory errors (typical Inertial Units fluctuations were longer in time than the typical integration time needed for these resolutions) and images were synthesized again with corrected trajectory [1].

High resolution (10 cm) SAR imaging initiated in year 2000 at ONERA requires autofocus for estimating velocity error fluctuations much shorter than the integration time thus an autofocus based on multilateration from phase tracking of point-like reflectors was designed [2] with automatic detection of the appropriate stable point-like reflexion on the ground. This algorithms uses range-clipped and narrow Doppler-band filtered profiles around the point-like reflexion to measure and unwrap the echo phase. From these phase variation measurement in at least three independent directions for any point of the acquisition trajectory, an accurate trajectory update can be derived.

With circular SAR imaging with high banking angle and bistatic SAR imaging, (and some wild remote areas without enough appropriate man-made opportunistic reflectors) this autofocus method failed. The reason for circular SAR is that high banking angle masks GPS satellites thus ruins GPS hybridizing, raising the Doppler dither of the point echoes which implied widening the Doppler filter hence possibly mixing the tracked point echo with neighbouring echoes. For bistatic SAR, very few (if any) point-like echoes are usually present due to the fact that 90°corner (present in many man made landscape features) scatter the radiowaves back to the transmitter and not to the sensor when there is any significant bistatic angle. Furthermore, true bistatic autofocus (not relying on reference monostatic image as in [3]) need more independent directions for multilateration since one extra time coordinate (the Local Oscillator drift) must be retrieved.

2 Algorithm principle

Instead of following the phase of point-like reflectors, the new algorithm makes small images in the ranging directions for adjacent sub-apertures and measures the position drift between the images that can be related to elevation and velocity errors. The main drawback of this map-drift approach is the insensitivity of the measurement to motion error at time scale under the sub-aperture duration.

In order to dodge this problem, a coarse-to-fine organising is used, starting from short sub-apertures yielding the high frequency corrections (with low image resolution hence low accuracy) to longer and longer sub-apertures yielding with higher and higher accuracy the low frequency corrections.

2.1 Derivation of errors from displacements

Each successive local image is correlated with the multi-look local image (incoherent sum of the previous and reg-

istered images with a decay factor). A decay factor of 1 (without decay) is allowed and sometimes very useful as for forcing a circular flight trajectory to "close" (*i.e.* match after each turn).

Velocity correction(s) are computed for each centre of integration by solving the linearised correction → apparent displacement equation set. Unknown are at each integration centre 0 to 3D trajectory correction and/or 1D time (LO drift) correction. (1D trajectory means in the radial average direction of the targets, 2D means horizontal plane correction).

Optionally, a near-range bias and target altitude biases may be added in the unknown set. In case 3D trajectory is evaluated without target altitude biases, an initial vertical trajectory correction is added, and if 2 or 3D <u>bistatic</u> trajectory correction is evaluated also 2 horizontal initial receiver trajectory corrections are added (this changes the initial bistatic separation which is not translation invariant).

Since the linear set of equation is large (especially for the first iterations when the sub-aperture time is short) and ill-conditioned in general its resolution is done by singular value decomposition (SVD) to avoid numerical instability. To give an idea of the equation set, in the monostatic case, if radial and perpendicular apparent local image displacement are denoted Δr and Δz, in monostatic case the linearised equations for H target altitude error, r_o near-range error, R_x, R_y, R_z the sensor position error, v_{rad} the radial velocity error and v_{r_o} the L.O. drift (useless indeed in monostatic case) are:

$$\partial \Delta r / \partial H = tg(\eta) \qquad \partial \Delta z / \partial v_{rad} = -1/cos(\eta)\dot{\xi}$$
$$\partial \Delta r / \partial r_o = -1/cos(\eta) \quad \partial \Delta z / \partial H = -\dot{\eta}/(cos(\eta))^2\dot{\xi}$$
$$\partial \Delta r / \partial R_x = -sin(\xi) \quad \partial \Delta z / \partial r_o = tg(\eta)\dot{\eta}/cos(\eta)\dot{\xi}$$
$$\partial \Delta r / \partial R_y = -cos(\xi) \quad \partial \Delta z / \partial R_x = cos(\xi)$$
$$\partial \Delta r / \partial R_z = -tg(\eta) \quad \partial \Delta z / \partial R_y = -sin(\xi)$$
$$\partial \Delta z / \partial R_z = \dot{\eta}/(cos(\eta))^2\dot{\xi}$$

$\partial \Delta z / \partial v_{r_o} = 1/cos(\eta)\dot{\xi}$ (useless for monostatic case)

The bistatic case is more complicated since the separate heading and elevation angles of the transmitter (ξ_T, η_T) and receiver (ξ_R, η_R) are required and not only their bistatic values (ξ, η) that of the V mean of the unit vectors U_T and U_R.

$\partial \Delta r / \partial H = (sin(\eta_T) + sin(\eta_R))/(cos(\xi_T - \xi)cos(\eta_T) + cos(\xi_R - \xi)cos(\eta_R))$

$\partial \Delta r / \partial r_o = -2/(cos(\xi_T - \xi)cos(\eta_T) + cos(\xi_R - \xi)cos(\eta_R))$

$\partial \Delta z / \partial v_{rad} = -1/(cos(\xi_T - \xi)cos(\eta_T)\dot{\xi}_T + cos(\xi_R - \xi)cos(\eta_R)\dot{\xi}_R - sin(\xi_T - \xi)sin(\eta_T)\dot{\eta}_T - sin(\xi_R - \xi)sin(\eta_R)\dot{\eta}_R)$

v_{rad} is the receiver velocity error, hence the 1/2 factor that appears here if we let $R = T$ compared with monostatic case.

$\partial \Delta z / \partial H = -((sin(\eta_T) + sin(\eta_R))(cos(\xi_T - \xi)sin(\eta_T)\dot{\eta}_T + cos(\xi_R - \xi)sin(\eta_R)\dot{\eta}_R + sin(\xi_T - \xi)cos(\eta_T)\dot{\xi}_T + sin(\xi_R - \xi)cos(\eta_R)\dot{\xi}_R)/(cos(\xi_T - \xi)cos(\eta_T) + cos(\xi_R - \xi)cos(\eta_R)) + cos(\eta_T)\dot{\eta}_T +$

$cos(\eta_R)\dot{\eta}_R)/(cos(\xi_T - \xi)cos(\eta_T)\dot{\xi}_T + cos(\xi_R - \xi)cos(\eta_R)\dot{\xi}_R - sin(\xi_T - \xi)sin(\eta_T)\dot{\eta}_T - sin(\xi_R - \xi)sin(\eta_R)\dot{\eta}_R)$

$\partial \Delta z / \partial r_o = 2(cos(\xi_T - \xi)sin(\eta_T)\dot{\eta}_T + cos(\xi_R - \xi)sin(\eta_R)\dot{\eta}_R + sin(\xi_T - \xi)cos(\eta_T)\dot{\xi}_T + sin(\xi_R - \xi)cos(\eta_R)\dot{\xi}_R)/((cos(\xi_T - \xi)cos(\eta_T) + cos(\xi_R - \xi)cos(\eta_R))(cos(\xi_T - \xi)cos(\eta_T)\dot{\xi}_T + cos(\xi_R - \xi)cos(\eta_R)\dot{\xi}_R - sin(\xi_T - \xi)sin(\eta_T)\dot{\eta}_T - sin(\xi_R - \xi)sin(\eta_R)\dot{\eta}_R))$

$\partial \Delta z / \partial v_{ro} = 2/(cos(\xi_T - \xi)cos(\eta_T)\dot{\xi}_T + cos(\xi_R - \xi)cos(\eta_R)\dot{\xi}_R - sin(\xi_T - \xi)sin(\eta_T)\dot{\eta}_T - sin(\xi_R - \xi)sin(\eta_R)\dot{\eta}_R)$

The bistatic formulae for the position aberration due to cumulative sensor trajectory update (i.e. formulae for $\partial \Delta r / \partial R_x, \partial \Delta r / \partial R_y, \partial \Delta r / \partial R_z, \partial \Delta z / \partial R_x, \partial \Delta z / \partial R_y$ & $\partial \Delta z / \partial R_z$) are far from trivial (I gave up) and probably not very efficient from a computation viewpoint.

These values are instead computed numerically by expressing the effect on the range and Doppler of an aberration in apparent position and equating it to the effect on range and Doppler of a sensor position bias. This solves as an easy linear system of equation AX=B where A is a 2×2 matrix, X is the 3×2 unknown
$$\begin{bmatrix} \partial \Delta r / \partial R_x & \partial \Delta r / \partial R_y & \partial \Delta r / \partial R_z \\ \partial \Delta z / \partial R_x & \partial \Delta z / \partial R_y & \partial \Delta z / \partial R_z \end{bmatrix}$$ and B a 3×2 matrix.

For improving conditioning, Δr and Δz are measured from several spans of time (in particular, at short time only Δz is significant, while Δr builds up along cumulative variations of heading ξ) thus increasing the number of equations in the system (with little impact on the overall solving time dominated by SVD which depends on the number of unknowns).

2.2 Fast local image synthesis

Since the whole process requires synthesis of a large number of small SAR images around the ranging directions, the image synthesis speed is critical. This lead us to use polar format frequency domain synthesis, starting from range-limited and narrow Doppler-filtered profiles around the ranging points (indeed the same profiles used in the previous algorithm for following the phase of the point-like echoes). This PFA synthesis, derived from an early ISAR processor [4] and previously used for under foliage and very high resolution imaging of compact targets [5], have been adapted to bistatic acquisition mode.

The principle of the bistatic Polar Format Algorithm (PFA) illustrated in **Figure 1**, is that the path difference is the dot product of the two (solid and dashed) blue vectors $V = \frac{1}{2}(U_T + U_R)$ and P. Time domain integration is possible, but frequency domain is by far more efficient: A range profile offset by $H_{rec}sin(\eta)$ and contracted by the modulus of the projection of vector V on the reconstruction plane (*i.e.* $cos(\eta)cos(\beta/2)$ where η is the elevation of V above the horizontal and β the bistatic angle) is the orthogonal projection of the image in the direction ξ of V

projected on the horizontal plane.

Hence the Fourier transform of this profile, inversely scaled (and with a linear phase modulation for the offset) is a slice of the image spectrum. The scaling is made more accurate by zero-padding the range profile prior to FFT.

Once a set of range profile with ξ angle spanning the integration angle have been processed, they are sorted by ξ angle (sorting is only useful for air-to-air SAR where η and ξ are the elevation and heading from the target aircraft reference frame, and target attitude motion may cause ξ be non monotonic with time). Then the image spectrum is interpolated on a square grid, each point being interpolated between the two slices around its own heading angle. Eventually a 2D FFT yields the final image.
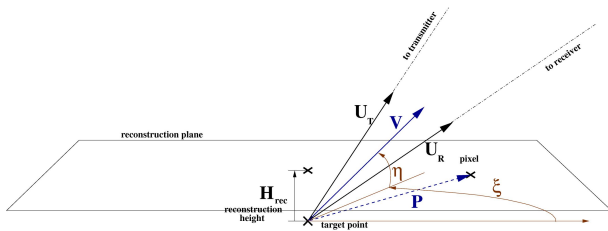

Figure 2: Four target areas selected on a single flash-look bistatic SAR image (red circles).

Figure 1: principle of the bistatic Polar Format Algorithm. U_T and U_R are unit vectors to transmitter and receiver, V and P are non unit vectors.

Figure 3: the corresponding four filtered range profiles (stacked) range from top to bottom, time from left to right.

3 Results

The conjunction of fast PFA and local map-drift allowed bistatic SAR imaging with autofocus without use of the corresponding monostatic images (previous bistatic images obtained at ONERA used local frame drift autofocus between a monostatic and a bistatic full resolution stripmap image to retrieve the L.O. clock drift).

The process is illustrated with a bistatic acquisition with RAMSES transmitting at X-band while flying North at a velocity of 150 kt and an altitude of 5000 ft and a Stemme touring motor glider as receiver flying 30Â° to the West at a velocity of 96 kt and an altitude of 3600 ft.
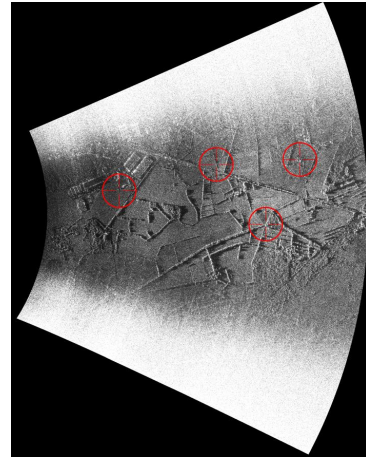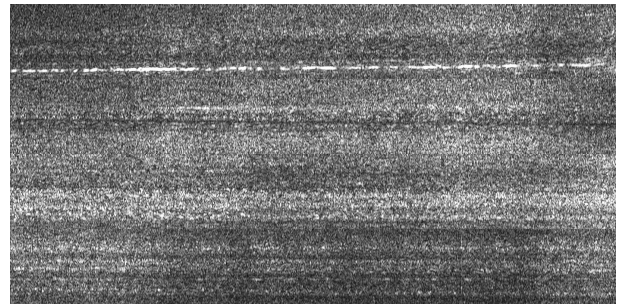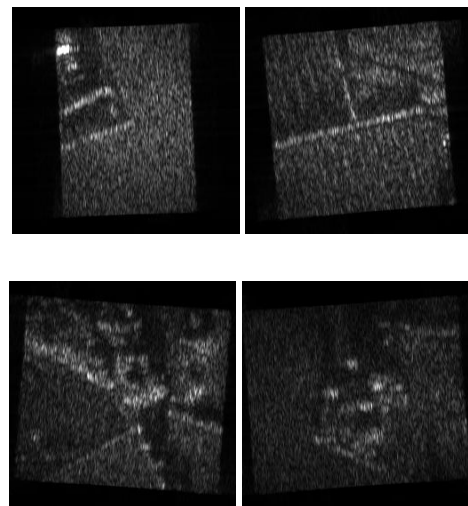

Figure 4: Four corresponding SAR images synthesized by the bistatic PFA processor.
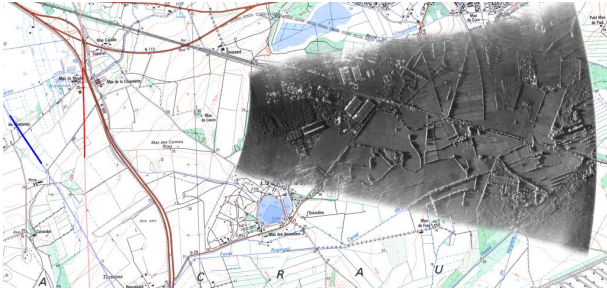
Figure 5: final 23-look bistatic SAR image with non-parallel, different velocities. Transmitter trajectory in red and sensor trajectory in blue

Figure 6: detail of **Figure 5**

Figure 7: simultaneous monostatic 23-look image of the same area for comparison

4 Spinouts and future works

As unexpected spinouts, this autofocus allowed allowed our first successful air-to-air high resolution ISAR imag-ing: an opportunity imaging of the receiving aircraft (a Stemme TMG) from the transmitting one (RAMSES) dur-ing a bistatic experiment (see **Figure 8**) This image used first the autofocus described above for determination of the relative trajectory of the target aircraft centre, and then sub-targets (nose and wings tips) were tracked to retrieve accu-rate target aircraft attitude yielding high resolution image in the target reference coordinates (detail of this processing is given in a dedicated paper in this conference).
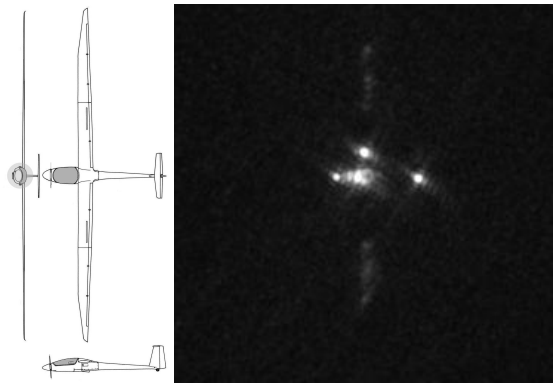

Figure 8: 3 view blueprint of the imaged aircraft (with-out the radar pod under right wing) and 15-look air-to-air ISAR image from RAMSES

Present work under progress, is the automatic determina-tion of the targets area from a first (poorly focused) image in the same manner the point-like reflections are auto-matically detected in the previous production-line phase tracking autofocus.

References

[1] Nahum, C. : *Autofocus using Multi-Scale Local Cor-relation*, Europto Symposium Aerospace Remote Sensing : Barcelona Spain, 1989

[2] Cantalloube, H.; Dubois-Fernandez, P.: *Airborne X-band SAR imaging with 10 cm resolution: technical challenge and preliminary results*, IEE Proc RSN 153, (2006) 163 - 176

[3] Cantalloube, H.; Wendler, M.; Giroux, V.; Dubois-Fernandez, P.; Krieger, G.: *Challenges in SAR pro-cessing for airborne bistatic acquisitions*, EUSAR conference : Ulm Germany, 2004

[4] Cantalloube, H.; Nahum, C.: *Autofocus of (inverse) synthetic aperture radar for motion compensation*, Nat. Aerospace & Electr. conference : Dayton Ohio USA, 1996

[5] Cantalloube, H.; Colin É.: *Airborne SAR imaging along a circular trajectory*, EUSAR conference : Dresden Germany, 2006